International Journal of Hydrogen Energy 54 (2024) 665–677

Contents lists available at ScienceDirect

International Journal of Hydrogen Energy

journal homepage: www.elsevier.com/locate/he

Exploring the hydrogen and methane storage capacities of novel DUT MOFs at room temperature: A Grand Canonical Monte Carlo simulation study

A. Granja-DelRío, I. Cabria *

Departamento de Física Teórica, Atómica y Óptica, Universidad de Valladolid, ES-47011 Valladolid, Spain

ARTICLE INFO

Keywords:
Hydrogen storage
Methane storage
Metal-organic frameworks
Grand Canonical Monte Carlo simulations

ABSTRACT

Metal-Organic Frameworks (MOFs) are a significant and promising category of solid that have garnered substantial attention for their potential in storing hydrogen and methane. Grand Canonical Monte Carlo (GCMC) simulations of the usable hydrogen and methane storage capacities of five DUT MOFs (Dresden University of Technology), based on tritopic ligands and copper, have been carried out at room temperature and pressures between 0.5 and 35 MPa. These DUT MOFs exhibit high usable hydrogen and methane storage capacities, comparable or higher than the storage capacities of the best classical MOFs and the best Cu-based MOFs. The usable methane gravimetric storage capacities at 35 MPa and room temperature of these DUTs reach the Department of Energy (DOE) methane gravimetric target and their usable volumetric capacities are close to the DOE methane volumetric target.

1. Introduction

Human well-being has led to negative environmental impacts on the planet's health. Fossil fuel combustion produces greenhouse gases which directly affect to climate change, pollution, ocean acidification and resource depletion due to unsustainable extraction and consumption of natural resources. In recent decades, several efforts have been made to explore alternative approaches to substitute fossil fuels. Since transport is one of the principal contributors to environmental threats, hydrogen arises as an important candidate to replace gasoline as a fuel in cars with the advantage of the absence of CO_2 emissions. Hydrogen can play an essential role to meet the net-zero CO_2 emissions by 2050.

Hydrogen is an energy vector attractive for vehicles [1–3]. However, its storage at room temperature and moderate pressures still remains as an important goal [4–6]. The current on-board hydrogen storage involves the use of compressed gas technology. However, this method poses challenges related to cost, volume, and safety. Ongoing research and development efforts are focused on exploring alternative storage technologies, such as physisorption on solid porous materials. The goal is to find an on-board hydrogen storage system such that the hydrogen vehicle has the same autonomy range as the current fossil fuel-based vehicles.

The DOE has set two main goals to be accomplished before 2025 for an on-board hydrogen storage system: 0.040 kg H_2/L and 5.5 wt. % for the volumetric and gravimetric storage capacities, respectively [7,8]. These values represent the usable, often referred to as delivery or working, capacities of the hydrogen storage system. They signify the amount of hydrogen that can be effectively utilized for automotive applications and providing an autonomy of about 600 km. Furthermore, these targets also align with the concept of reversible storage, meaning that the stored hydrogen can be released and replenished repeatedly. Besides that, whereas advancements in hydrogen-powered vehicle technology takes place, it seems necessary a temporary bridge between gasoline-powered automobiles and the widespread adoption of hydrogen-based vehicles [9].

Natural gas seems to be that possible temporary bridge, due to its extensive distribution, abundant reserves, low cost and relatively cleaner nature compared to oil. The motivation is that the predominant component of natural gas is methane and it possesses the highest hydrogen-to-carbon ratio among all fossil fuels. When compared to coal, natural gas has the potential to significantly reduce CO_2 emissions by approximately 50%, reaching the emission goals of the European Union: 95 g of CO_2/km. Methane exhibits a higher gravimetric capacity than gasoline, which makes it a promising option for energy storage [10,11].

In order to advance the field of methane storage, the Advanced Research Projects Agency-Energy (ARPA-E) of the DOE has established specific targets for on-board usable methane storage: a volumetric capacity of 0.250 kg of methane per liter and a gravimetric capacity of 0.5 g/g or 33.33 wt. % at room temperature and low or moderate pressures [10–14]. Apart from compression and liquefaction, another method of storing methane is solid storage. The last one involves

* Corresponding author.
E-mail address: ivan.cabria@uva.es (I. Cabria).

https://doi.org/10.1016/j.ijhydene.2023.11.258
Received 26 September 2023; Received in revised form 16 November 2023; Accepted 22 November 2023
Available online 30 November 2023

utilizing solid porous materials for physisorption, where the gases are adsorbed inside the pores of the material. This storage method provides more stored gas at low and moderate pressures (≤25–35 MPa) than the compressed method [12,15]. In an Adsorbed Natural Gas (ANG) storage system, the tanks are filled with a solid porous material that stores the gas inside its pores.

The ongoing research in on-board gas storage using different groups of solid porous materials is concentrated on identifying materials capable of storing a sufficient quantity of hydrogen or methane at room temperature and low or moderate pressures [16–31]. In recent decades, extensive research efforts have been dedicated to the utilization of MOFs as gas storage materials for adsorbed hydrogen and natural gas [32–41]. MOFs are characterized by their high porosity and are composed of metal ions or metal-containing clusters (secondary building blocks) connected by organic ligands forming 2D or 3D structures [42]. The great abundance of organic linkers and the wide range of metal ions and clusters available enables the creation of numerous MOFs variations with tunable properties and makes them an attractive choice for efficient gas storage applications [43].

Adsorption properties of MOFs [44], including storage capacities for hydrogen and methane, have been extensively studied through a combination of experiments [45–48] and simulations [49–58], which include the widely used GCMC method [59–61]. Monte Carlo simulations, widely employed in the literature, have demonstrated their capability to predict the adsorption properties of numerous molecules on existing MOFs.

A group of the Dresden University of Technology published the synthesis of five DUT MOFs [62] with tritopic ligands. These ligands can be functionalized to tune the properties of the MOFs for gas storage, among other applications. The only metal of the five DUTs is copper, which makes these materials relatively cheap to synthesize.

The purpose of this investigation is to predict and analyze the hydrogen and methane storage capacities of these DUT MOFs with promising potential as storage materials. GCMC simulations have been employed to simulate and evaluate the storage capacities of the five synthesized DUT MOFs at room temperature and pressures between 0.5 and 35 MPa. A comparative analysis has been conducted to study the storage capacities of these materials with Cu-based MOFs, as well as a selection of well-known and established classical MOFs. Furthermore, the storage capacities of all simulated MOFs have been analyzed as a function of their porosity, density and pore size. Understanding and predicting the interactions between the adsorbed molecule and MOF are crucial for designing new metal–organic frameworks.

2. Methodology

2.1. Simulations parameters and details

GCMC simulations to obtain hydrogen and methane adsorption isotherms of DUT-63, DUT-64, DUT-77, DUT-78 and DUT-79 MOFs [62] have been carried out at room temperature, 298.15 K, and pressures in a range between 0.5 and 35 MPa. Ten million iterations were performed for each GCMC simulation. To reach the equilibrium, five million iterations were calculated. The rest of the iterations were employed to find gravimetric and volumetric storage capacities for both: hydrogen and methane. In order to compare storage capacities, GCMC simulations of the storage capacities of a set of 23 classical MOFs and a set of nine selected Cu-based MOFs with C/Cu ratios identical to the C/Cu ratios of the DUTs were performed at the same temperature and pressure conditions as mentioned above.

Simulations have been carried out using an in-house code, named mcmgs. The Metropolis algorithm was used in each iteration [63]. The possible changes or moves consisted as follows: 20% of the trials involved the movement of a molecule, 40% for the deletion of one molecule and another 40% for the insertion of one molecule. Many tests were performed to obtain these percentages.

Table 1
Parameters of the SRK equation of state of hydrogen and methane: ω, P_c in MPa and T_c in K.

Gas	ω	P_c	T_c	Source
H_2	−0.216	1.28	33.2	[65]
CH_4	0.01142	4.5992	190.56	[66]

Table 2
Lennard-Jones coefficients σ and ϵ of the molecules and of the atoms of the MOFs studied in the present GCMC simulations.

Atom or molecule	σ (Å)	ϵ (eV)	Source
Al	2.574	0.507220	Filippova et al. [75]
Br	3.519	0.016043	Mayo et al. [76]
C	3.400	0.003744	Tu et al. [77]
Cu	2.297	0.520310	Filippova et al. [75]
H	2.846	0.000659	Mayo et al. [76]
H_2	2.970	0.002870	Rzepka et al. [70]
N	3.310	0.003214	Cheung et al. [78]
O	3.033	0.004150	Mayo et al. [76]
CH_4	3.730	0.012748	Jorgensen et al. [79]
S	3.590	0.014916	Mayo et al. [76]
Zn	0.998	0.008291	Soper et al. [80]
C-H_2	3.190	0.002628	Rzepka et al. [70]

The chemical potential used in GCMC simulations was derived from the Soave–Redlich–Kwong, SRK [64], equation of state. Values for the dimensionless acentric factor ω, the critical pressure P_c and the critical temperature T_c of hydrogen and methane were taken from Zhou and Zhou [65] and Xu et al. [66], respectively. These values can be found in Table 1.

Lennard-Jones (LJ) interaction potential energies [67] have been used to simulate the interactions between gas molecules (H_2 or CH_4) and between the atoms of the MOFs and the gas molecules. LJ interaction potential follows the next equation:

$$V = 4\epsilon\left[\left(\frac{\sigma}{r}\right)^{12} - \left(\frac{\sigma}{r}\right)^{6}\right], \quad (1)$$

where ϵ in Eq. (1) is the minimum value of LJ interaction potential energy ($\epsilon > 0$), σ is the distance at which the interaction between the two particles is zero and r is the distance between the two particles. The values of the ϵ and σ coefficients depend on each particle involved in the interaction. The ϵ and σ coefficients of the interactions between different particles have been obtained using the Berthelot [68] and the Good–Hope [69] combining rules, respectively.

Table 2 shows the values for ϵ and σ coefficients of the atoms and molecules used in the present GCMC simulations. The LJ coefficients of the C-H_2 interaction used in these simulations were obtained from Rzepka et al. [70]. The LJ parameters of the rest of the interactions have been obtained by means of the above-mentioned Good–Hope–Berthelot combining rule. To include quantum effects in the interaction potential, the Feynman–Hibbs correction has been used [71]. All the present GCMC simulations have been performed using this quantum correction. The cutoff radius for the LJ interaction potential was set at 20 Å for interactions involving H_2 and 7.5 Å for CH_4. These specific values were determined through multiple tests as referenced in previous studies [72,73]. Furthermore, a similar value of 9 Å for methane was reported by Docherty et al. [74].

During a GCMC simulation, the simulation cell was replicated in a spatial direction a number of times equal to ceiling(r_c/m), where r_c is the cutoff radius and m is the length of the simulation cell in that direction. This means that the simulation is replicated at least one time in any direction, to avoid boundary effects in the limits of the cell. If the cutoff radius is larger than the length of a simulation cell along a spatial direction, then the simulation cell was replicated two or more times in that direction.

Table 3
P_{mcmgs}, P_{zeo++}, and the difference ΔP between them of the DUTs, the selected Cu-based and the classical MOFs.

MOF	P_{mcmgs}	P_{zeo++}	ΔP	MOF	P_{mcmgs}	P_{zeo++}	ΔP
BINROH	0.430	0.506	−0.076	IRMOF-4	0.102	0.146	−0.044
BIPSUQ	0.519	0.590	−0.071	IRMOF-5	0.030	0.016	0.014
DUT-63	0.772	0.820	−0.048	IRMOF-6	0.303	0.399	−0.096
DUT-64	0.715	0.778	−0.063	IRMOF-7	0.115	0.113	0.002
DUT-77	0.664	0.732	−0.068	IRMOF-8	0.559	0.611	−0.052
DUT-78	0.641	0.700	−0.059	IRMOF-9	0.334	0.399	−0.065
DUT-79	0.581	0.656	−0.075	IRMOF-11	0.585	0.628	−0.043
ENIHUG01	0.372	0.454	−0.082	IRMOF-12	0.585	0.653	−0.068
NIGDIS	0.354	0.439	−0.085	IRMOF-14	0.582	0.663	−0.081
OGEBAF01	0.463	0.523	−0.060	IRMOF-15	0.861	0.756	0.105
OGEBAF	0.464	0.523	−0.059	IRMOF-16	0.628	0.679	−0.051
PODKOK	0.450	0.531	−0.081	IRMOF-18	0.274	0.377	−0.103
YOPSUS	0.143	0.172	−0.029	IRMOF-20	0.535	0.598	−0.063
ZILFOR	0.331	0.416	−0.085	MOF-177	0.562	0.640	−0.078
IRMOF-1	0.431	0.534	−0.103	NU-111	0.528	0.598	−0.070
IRMOF-2	0.213	0.253	−0.040	NU-125	0.393	0.479	−0.086
IRMOF-3	0.364	0.447	−0.083	ZIF-8	0.206	0.252	−0.046

Table 4
Largest pore radius R_l, largest included sphere radius R_i, and the difference ΔR between them (in Å) of the DUTs, the selected Cu-based and the classical MOFs.

MOF	R_l	R_i	ΔR	MOF	R_l	R_i	ΔR
DUT-63	17.88	16.36	1.52	IRMOF-4	7.00	5.36	1.64
DUT-64	14.32	13.13	1.19	IRMOF-5	3.95	2.72	1.23
DUT-77	13.68	12.59	1.09	IRMOF-6	8.89	7.52	1.37
DUT-78	13.10	12.43	0.67	IRMOF-7	5.33	4.05	1.28
DUT-79	12.65	12.65	0.00	IRMOF-8	10.38	8.96	1.42
BINROH	10.58	10.66	−0.08	IRMOF-9	6.85	5.56	1.29
BIPSUQ	10.28	9.31	0.97	IRMOF-11	11.20	9.82	1.38
ENIHUG01	8.27	6.89	1.38	IRMOF-12	11.58	10.16	1.42
NIGDIS	8.13	6.97	1.16	IRMOF-14	11.90	10.47	1.43
OGEBAF01	7.87	6.62	1.25	IRMOF-15	12.99	11.86	1.13
OGEBAF	7.82	6.72	1.10	IRMOF-16	11.61	10.07	1.54
PODKOK	10.00	9.24	0.76	IRMOF-18	8.40	7.12	1.28
YOPSUS	5.04	3.64	1.40	IRMOF-20	10.12	8.64	1.48
ZILFOR	5.65	4.65	1.00	MOF-177	9.99	8.49	1.50
IRMOF-1	9.12	7.53	1.59	NU-111	12.12	10.91	1.21
IRMOF-2	8.17	6.41	1.76	NU-125	11.27	9.69	1.58
IRMOF-3	9.02	7.49	1.54	ZIF-8	7.39	6.62	0.77

2.2. Calculation of the porosity

The porosity is defined as the ratio of the available volume and the volume of the simulation cell of a MOF. It is a dimensionless magnitude. The available volume for a gas molecule is the difference between the volume of the simulation cell, V, and the volume occupied by the atoms of the MOF, V_{occ}.

The volume V_{occ} is calculated creating a grid of n points in the simulation cell. ni is the number of grid points inside the sphere of an atom of the simulation cell. Then, the volume V_{occ} is determined by Vni/n. The radius r of an atom is equal to $\sigma(atom, molecule)$ and the volume of the sphere of an atom is $4\pi r^3/3$. The LJ interaction potential energy is zero at an atom–molecule distance equal to $\sigma(atom, molecule)$. The available volume, the volume occupied by the atoms and the porosity depend on the type of gas molecule, due to this definition of the radius of an atom interacting with a molecule.

The Zeo++ code [81] has been used to calculate the accessible volume. Zeo++ calculates the Voronoi network using Voronoi decomposition. The obtained Voronoi network represents the empty spaces within the structure. Analyzing this network provides valuable insights into key features, including details about the largest opening in the material, the maximum size of a spherical probe capable of moving through the structure unobstructed, the topology of channel systems, and other relevant parameters. The code provides access to various structural features, specifically, it allows the determination of the accessible volume which is defined as the volume available to the center of a spherical probe [82].

The calculation of the porosity using the Zeo++ has been performed as the fraction accessible volume/simulation cell volume, to ensure consistency with the concept of porosity as defined in this work. Table 3 presents the calculated porosity for each MOF using the algorithm described above, P_{mcmgs}, using the Zeo++ code, P_{zeo++}, and the difference between these two porosities, ΔP. The difference is very small.

2.3. Calculation of the pore radius

The MOFs were analyzed using an algorithm to find the pores with a radius equal to or greater than 3 Å. Pores with a smaller radius cannot accommodate hydrogen or methane molecules. The algorithm starts by generating a three-dimensional grid of points within the simulation cell. The distance between the grid points is 1.0 Å. In the next step the algorithm calculates, for each grid point i, the distance d_{ij} from point i to each atom j in the cell. The minimum distance of the d_{ij} set of distances, $dmin(i)$, is calculated for each grid point i of the grid.

The algorithm calculates in the third step the pore radius as follows: the radius of the initial or first pore is the largest value of the set of $dmin(i)$ values, with the corresponding grid point i as the center of the pore. The set of $dmin(i)$ values is then recalculated. The grid points contained within the first pore are treated as 'atoms' within the MOF structure. The second and third steps are repeated to obtain a new set of $dmin(i)$ values and to find a second, a third pore, etc. This process continues until the largest value among all $dmin(i)$ values is smaller than 3 Å. Hence, the algorithm finds a set of pore radii, along with the average pore radius. The initial pore radius obtained using this algorithm corresponds to the largest pore radius of the MOF. The spherical pores obtained using this algorithm do not overlap.

The Zeo++ code [81] has been also used to calculate the pore radii. As previously mentioned, different structural descriptors can be obtained from the code, specifically, the radii of the largest included sphere and the largest free sphere, which are simple parameters describing the geometry of the channel system in porous materials. The largest included sphere indicates the position of the most sizeable cavity within a porous material and measures its dimensions. Conversely, the largest free sphere corresponds to the most substantial spherical probe capable of diffusing through a structure and measures the smallest constraining opening along a diffusion path [83].

Table 4 shows the largest pore radius R_l of each MOF calculated in this work using the algorithm explained above, the radius of the largest included sphere R_i of each MOF determined using the Zeo++ code and the difference between these two radii. The greatest discrepancy is about 1.76 Å for IRMOF-2. Therefore, the pore size obtained from both codes is quite similar. The observed difference is not very significant and is likely due to the definition of the atomic radii and the interaction parameters of the LJ potential.

2.4. Definitions of the storage capacities

Total (hydrogen and methane) gravimetric and volumetric storage capacities [2,4,38] have been measured in the GCMC simulations. The volumetric storage capacity, v_c, at P and T, also called density of stored (hydrogen or methane), is defined by

$$v_c(P,T) = \frac{M_g(P,T)}{V}, \tag{2}$$

where V is the volume of the simulation cell and $M_g(P,T)$ is the mass of gas (hydrogen or methane) stored in the simulation cell at P and T. In this paper, v_c is calculated in kg of gas (hydrogen or methane) per liter. The total (hydrogen or methane) gravimetric storage capacity, g_c, at P and T is defined by

$$g_c(P,T) = \frac{100 M_g(P,T)}{M_g(P,T) + M_{ads}}, \tag{3}$$

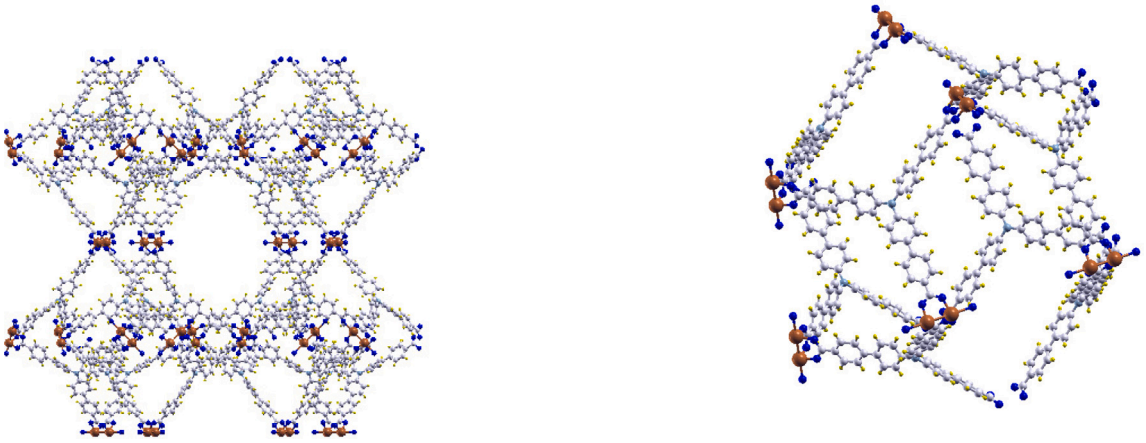

Fig. 1. Simulation cells of DUT-63 and 64 (left and right panels, respectively). Oxygen, carbon, hydrogen and copper atoms are represented by blue, gray, yellow and red balls, respectively. (For interpretation of the references to color in this figure legend, the reader is referred to the web version of this article.)

where M_{ads} is the mass of the adsorbent solid porous material of the simulation cell. Thus, the units of the total gravimetric capacity are calculated in wt. % units.

The usable mass of gas (hydrogen or methane) stored at P and T, $M_{ug}(P,T)$, is the difference between the total mass of gas stored at P and T and the total mass of gas stored at the depletion, also called minimum pressure, back pressure or backpressure, P_{dep}, and at the same temperature T [2,7,8,38]

$$M_{ug}(P,T) = M_g(P,T) - M_g(P_{dep},T)\,. \tag{4}$$

The usable (hydrogen or methane) volumetric and gravimetric capacities at P and T are given by Eqs. (2) and (3) inserting the usable mass of gas stored at P and T, Eq. (4), instead of $M_g(P,T)$:

$$v_c(P,T) = \frac{M_{ug}(P,T)}{V}\,, \tag{5}$$

$$g_c(P,T) = \frac{100 M_{ug}(P,T)}{M_{ug}(P,T) + M_{ads}}\,. \tag{6}$$

Fuel cells can operate with a depletion pressure ranging from 0.1 to 0.5 MPa [84]. Throughout this paper, the depletion pressure, P_{dep}, is 0.5 MPa and only the usable storage capacities will be used and analyzed, unless otherwise indicated.

2.5. Simulation cells

The simulation cells of the 23 classical MOFs, the Cu-based MOFs and the DUTs have been obtained from their files in the Crystallographic Information File (CIF) format on the Crystallographic Database Centre (CCDC) database [85]. The simulation cells of two DUT MOFs have been plotted in Fig. 1. The set of 23 classical MOFs is composed by IRMOF-1 to IRMOF-20 (except 10, 13, 17 and 19), HKUST-1, MOF-177, NU-111, NU-125 and ZIF-8 (IRMOF: Isoreticular Metal-Organic Frameworks).

The MOF CCDC subset contains about 600 Cu-based MOFs. The C/Cu ratio of those Cu-based MOFs and of the five DUT MOFs [62] were calculated. The Cu-based MOFs with the same ratios as the DUT MOFs (26, 32, 11.67 and 13.67) were selected (See Table 6). The porosity and the density of the Cu-based MOFs with the indicated ratios were also calculated. Among all of them, the ones with porosity above 10% and density below 1.1 kg/L were chosen to make GCMC simulations and to compare their storage capacities with those of the five DUT MOFs. In general, MOFs with these values for the porosity and the density have high storage capacities. These selections generated a set of nine Cu-based MOFs. The CCDC database identifiers of the nine selected Cu-based MOFs are: BINROH with ratio 26, BIPSUQ, OGEBAF and OGEBAF01 with ratio 11.67, ENIHUG01, NIGDIS, PODKOK and ZILFOR with ratio 13.67 and YOPSUS with ratio 32.

Table 5
Total hydrogen and methane storage capacities of some classical MOFs at different temperatures and pressures. Results include RASPA simulations and experimental values from other groups. Mcmgs values are obtained from simulations calculated in this work. Pressure P is in MPa, temperature T in K, gravimetric capacity g_c in wt. % and v_c in kg/L. Type means the type of capacity.

MOF	Gas	P	T	Technique	g_c	v_c	Type	Source
IRMOF-1	H_2	10	298	RASPA	1.35	0.0094	Total	[86]
IRMOF-1	H_2	10	298	mcmgs	1.14	0.0069	Total	
IRMOF-1	H_2	6	300	exps.	0.30		Excess	[87]
IRMOF-1	H_2	6	300	mcmgs	0.37		Excess	
IRMOF-1	CH_4	3.6	300	exps.	13.5	0.0787	Total	[87]
IRMOF-1	CH_4	3.6	300	mcmgs	12.3	0.0837	Total	
IRMOF-1	CH_4	4.5	298	RASPA	12.3		Total	[88]
IRMOF-1	CH_4	4.5	298	mcmgs	14.7		Total	
MOF-177	CH_4	10	298	exps.	22.0		Total	[89]
MOF-177	CH_4	10	298	mcmgs	26.6		Total	
HKUST-1	CH_4	6.5	298	exps.	17.8	0.1910	Total	[90]
HKUST-1	CH_4	6.5	298	mcmgs	15.4	0.1724	Total	
HKUST-1	CH_4	6.5	298	exps.	15.1	0.1574	Excess	[90]
HKUST-1	CH_4	6.5	298	mcmgs	14.8		Excess	
NU-125	CH_4	6.5	298	exps.	22.3	0.1659	Total	[90]
NU-125	CH_4	6.5	298	mcmgs	20.5	0.1570	Total	
NU-125	CH_4	6.5	298	exps.	18.2	0.1295	Excess	[90]
NU-125	CH_4	6.5	298	mcmgs	19.0		Excess	
Al-nia-MOF-1	CH_4	8	258	exps.	28.6	0.1880	Total	[91]
Al-nia-MOF-1	CH_4	8	258	mcmgs	29.1	0.2010	Total	[92]
Al-nia-MOF-1	CH_4	8	273	exps.	24.5	0.1660	Total	[91]
Al-nia-MOF-1	CH_4	8	273	mcmgs	27.6	0.1870	Total	[92]
Al-nia-MOF-1	CH_4	8	298	exps.	23.1	0.1420	Total	[91]
Al-nia-MOF-1	CH_4	8	298	mcmgs	24.8	0.1610	Total	[92]
Al-nia-MOF-1	CH_4	8	298	exps.	21.3	0.1230	Usable	[91]
Al-nia-MOF-1	CH_4	8	298	mcmgs	22.1	0.1390	Usable	[92]

2.6. Comparison of hydrogen and methane storage capacities with other simulation and experimental results

Total hydrogen and methane storage capacities of a compilation of classical MOFs are presented in Table 5. To assess these values, a comparison was made between simulations and experimental data from another research groups at similar ambient temperatures.

Concerning hydrogen, the total gravimetric and volumetric capacities calculated by the RASPA and mcmgs codes exhibit minimal differences. Specifically, mcmgs capacities are only around 20% and 36% smaller than the values obtained from the RASPA code for gravimetric and volumetric capacities, respectively. In the methane case, results comparing RASPA and mcmgs are quite similar as well as results comparing experiments and mcmgs values. For pressures below 10 MPa, experimental gravimetric capacities are only marginally higher than those derived from mcmgs simulations, by about 10%–15%. Similar

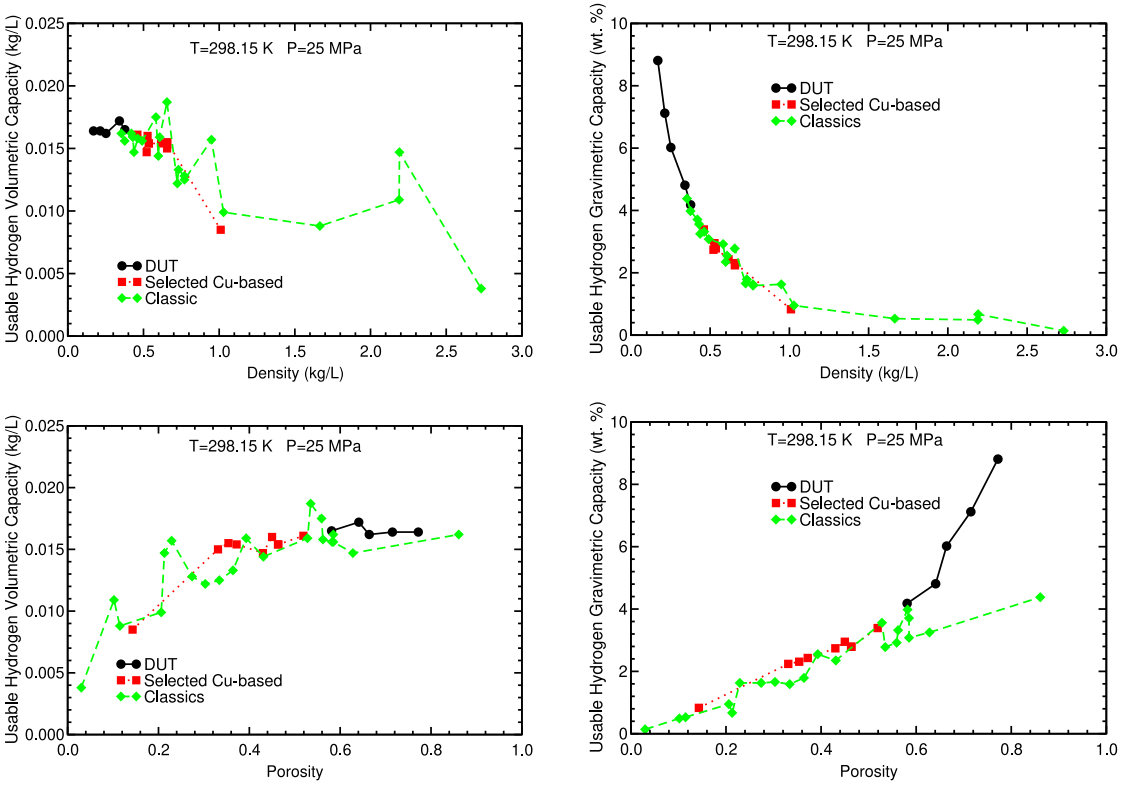

Fig. 2. Hydrogen gravimetric and volumetric usable capacity at 298.15 K and 25 MPa vs density and porosity.

Table 6
Hydrogen volumetric (in kg/L) and gravimetric (in wt. %) usable capacities at 298.15 K and 25 MPa obtained in the present GCMC simulations, C/Cu ratio, density (in kg/L), porosity and largest R_l and average R_{av} pore radius (Å) of the DUT and the selected Cu-based MOFs.

MOF	Ratio C/Cu	v_c	g_c	Density	Porosity	R_l	R_{av}
DUT-63	26	0.0164	8.81	0.170	0.772	17.88	15.90
DUT-64	26	0.0164	7.12	0.214	0.715	14.32	14.14
DUT-77	32	0.0162	6.02	0.252	0.664	13.68	13.46
DUT-78	11.67	0.0172	4.81	0.341	0.641	13.10	12.30
DUT-79	13.67	0.0165	4.18	0.377	0.581	12.65	4.39
BINROH	26	0.0147	2.74	0.521	0.430	10.58	4.00
YOPSUS	32	0.0085	0.83	1.010	0.143	5.04	3.86
BIPSUQ	11.43	0.0161	3.39	0.460	0.519	10.28	8.97
PODKOK	13.71	0.0160	2.95	0.527	0.450	10.00	5.80
ZILFOR	13.5	0.0150	2.24	0.656	0.331	5.65	4.92
NIGDIS	13.042	0.0155	2.31	0.658	0.354	8.13	5.60
ENIHUG01	13.500	0.0154	2.43	0.616	0.372	8.27	8.16
OGEBAF01	11.333	0.0154	2.79	0.535	0.463	7.87	6.86
OGEBAF	11.333	0.0154	2.79	0.536	0.464	7.82	6.65

differences are observed in the comparison between RASPA and mcmgs results for the total gravimetric capacity. The disparities between the total volumetric capacities obtained in the experiments and in the simulations with the mcmgs code are relatively small, around 10%.

3. Results

3.1. Hydrogen storage capacities

3.1.1. Hydrogen storage capacities as a function of porosity, density and pore size of DUT MOFs

The usable capacities of the five DUTs, the nine selected Cu-based and the 23 classical MOFs obtained in the GCMC simulations at 298.15 K and 25 MPa are plotted in Figs. 2 and 3 as functions of the density, porosity and pore size (largest and average pore size). Values for all these magnitudes can be found in Tables 6 and 7.

The capacities are inversely proportional to the density and directly proportional to the porosity. However, there are some MOFs which do not follow these tendencies. Furthermore, it is worth noting that in Fig. 2, the gravimetric and volumetric capacities of DUT MOFs lie along the general curve made by the gravimetric and volumetric capacities of classical and selected Cu-based MOFs as a function of the density. Hence, it could be possible to predict the usable gravimetric capacity of a DUT, using its density. On the other hand, DUT MOFs showed higher gravimetric capacity than classical MOFs for similar porosities. In addition, DUT MOFs presented slightly higher volumetric capacities than classical MOFs.

The dependence of the usable hydrogen storage capacities on the largest and average pore radius is plotted in Fig. 3. The usable gravimetric capacity increases linearly as the largest and average pore radius increases. As the pore radius increases, the density, in general, decreases and this, in turn, implies that the gravimetric capacity increases. This trend is, however, approximate and not accurate.

As regards the usable hydrogen volumetric capacity, the initial increase of the pore radius increases or favors the volumetric capacity, but then, there is some saturation effect and the volumetric capacity converges rapidly towards a constant value, as the pore radius increases. The usable volumetric capacity can be approximated by a function of the type $a - b/R$, where R is the largest pore radius R_l or the average pore radius R_{av}.

Classical MOFs with the highest and the lowest gravimetric and volumetric capacities at 25 MPa were chosen to compare with each DUT MOF in Tables 6 and 7. The five DUTs have four different C/Cu ratios. For each C/Cu ratio, the Cu-based MOF with the highest gravimetric and volumetric capacity at 25 MPa and room temperature was chosen from the group of nine selected Cu-based, to take part in the comparison in Tables 6 and 7. These are BINROH, which was reported as a gas storage and separation MOF [93], YOPSUS [94], BIPSUQ [95] and PODKOK [96]. The usable hydrogen storage capacities, C/Cu ratios, densities, porosities and pore sizes are compared in that table.

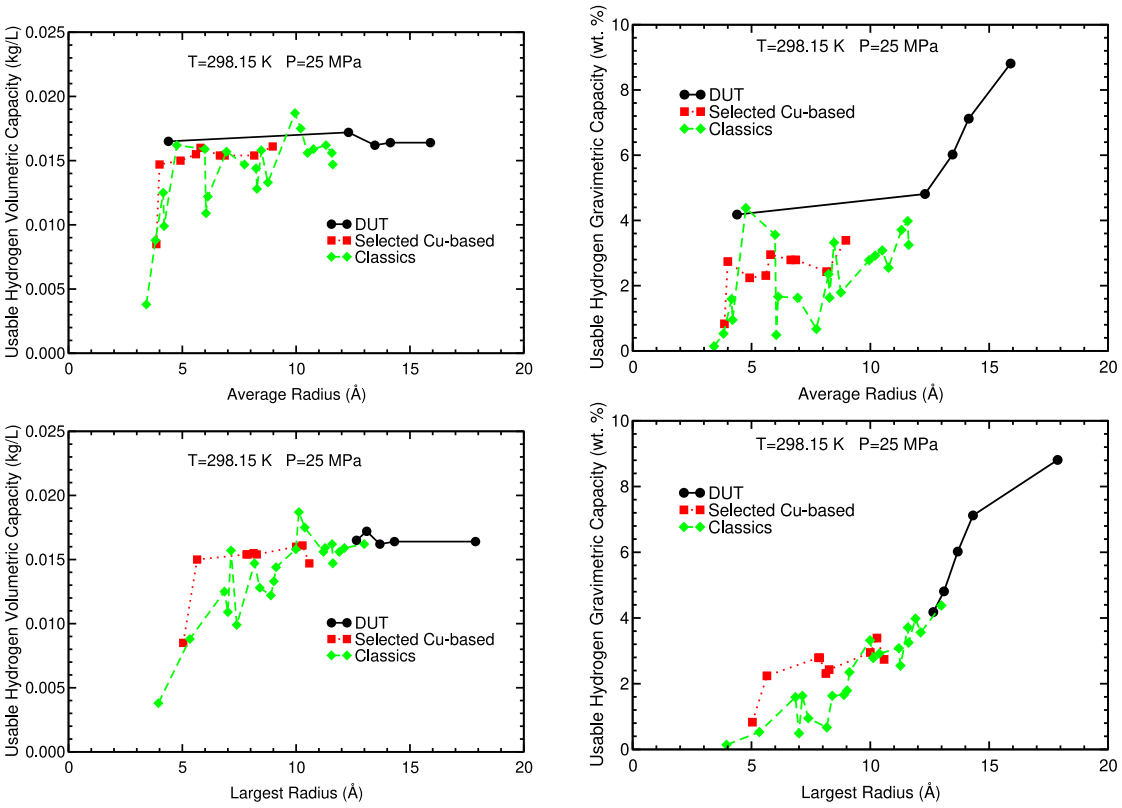

Fig. 3. Usable hydrogen gravimetric and volumetric usable capacity at 298.15 K and 25 MPa vs largest and average pore radius.

The DUTs, the best selected Cu-based MOFs and the classical MOFs, have similar usable volumetric capacities (0.015–0.017 kg/L), except YOPSUS. IRMOF-20 have the highest usable volumetric capacities, 0.0187 kg/L. If DUTs and best Cu-based MOFs with the same ratio are compared, then it can be noticed that the DUTs have higher usable gravimetric capacities. The DUTs have higher usable gravimetric capacities than the classical MOFs, except DUT-79.

Usable hydrogen storage capacities of DUT MOFs are between 4 and 9 wt. % for the gravimetric capacity and around 0.016–0.017 kg/L for the volumetric capacity, both at 298.15 K and 25 MPa (See Tables 6 and 7). DUT-63 MOF has the largest usable gravimetric capacity, but similar volumetric capacity as the other DUT MOFs.

3.1.2. Hydrogen storage capacities as a function of pressure

The usable storage capacities at 298.15 K of DUT MOFs are plotted in Fig. 4 as a function of the pressure between 0.5 and 35 MPa. DUT-63, 64, 77, 78 and 79 achieve the usable gravimetric DOE target (5.5% wt. [7]) at 298.15 K and 15, 20, 25, 30 and 35 MPa, respectively. Regarding the volumetric capacities (See Fig. 4), the usable volumetric capacities of the five DUT MOFs follow the same trend and have very similar values at 298.15 K and between 0.5 and 35 MPa. The highest value for each one is reached at 35 MPa and is about 0.022 kg/L. This value is about one half of the DOE volumetric target, 0.04 kg/L [7,8].

Figs. 5 and 6 provide a comparison of the gravimetric and volumetric usable capacities of DUTs and selected Cu-based MOFs with the same C/Cu ratio, and the classical MOFs with the lowest and highest storage capacities, IRMOF-5, 15 and 20, as the pressure varies. Each panel in those figures contains DUTs and one selected Cu-based MOF with the highest storage capacities and the same C/Cu ratio: 32, 26, 13.67 and 11.67 (See Tables 6 and 7).

It can be noticed in those Figures that, in general, DUTs and Cu-based MOFs with the same C/Cu ratio have similar volumetric usable capacities. DUTs have larger gravimetric usable capacities than the best Cu-based MOFs with the same C/Cu ratio. Compared with classical MOFs, DUTs and the classical MOFs have similar volumetric usable capacities. As regards gravimetric capacities, DUTs have larger gravimetric usable capacities than the classical MOFs, except DUT-79.

Table 7
Hydrogen volumetric (in kg/L) and gravimetric (in wt. %) usable capacities at 298.15 K and 25 MPa obtained in the present GCMC simulations, density (in kg/L), porosity and largest R_l and average R_{av} pore radius (Å) of the classical MOFs.

MOF	v_c	g_c	Density	Porosity	R_l	R_{av}
IRMOF-5	0.0038	0.14	2.731	0.030	3.95	3.42
IRMOF-15	0.0162	4.38	0.354	0.861	12.99	4.76
IRMOF-20	0.0187	2.78	0.655	0.535	10.12	9.95
IRMOF-1	0.0144	2.35	0.598	0.431	9.12	8.24
IRMOF-2	0.0147	0.67	2.191	0.213	8.17	7.73
IRMOF-3	0.0133	1.79	0.731	0.364	9.02	8.76
IRMOF-4	0.0109	0.49	2.189	0.102	7.00	6.04
IRMOF-6	0.0122	1.66	0.724	0.303	8.89	6.12
IRMOF-7	0.0088	0.53	1.665	0.115	5.33	3.82
IRMOF-8	0.0175	2.92	0.582	0.559	10.38	10.20
IRMOF-9	0.0125	1.59	0.771	0.334	6.85	4.16
IRMOF-11	0.0156	3.08	0.491	0.585	11.20	10.50
IRMOF-12	0.0162	3.71	0.420	0.585	11.58	11.31
IRMOF-14	0.0156	3.98	0.376	0.582	11.90	11.57
IRMOF-16	0.0147	3.25	0.437	0.628	11.61	11.61
IRMOF-18	0.0128	1.63	0.770	0.274	8.40	8.28
HKUST-1	0.0157	1.63	0.949	0.229	7.14	6.94
MOF-177	0.0158	3.32	0.462	0.562	9.99	8.47
NU-111	0.0159	3.56	0.430	0.528	12.12	5.99
NU-125	0.0159	2.55	0.607	0.393	11.27	10.76
ZIF-8	0.0099	0.95	1.029	0.206	7.39	4.20

3.2. Methane storage capacities

3.2.1. Methane storage capacities as a function of porosity, density and pore size of DUT MOFs

The usable methane storage capacities of the same MOFs have been also explored. The dependence of the usable methane storage capacities

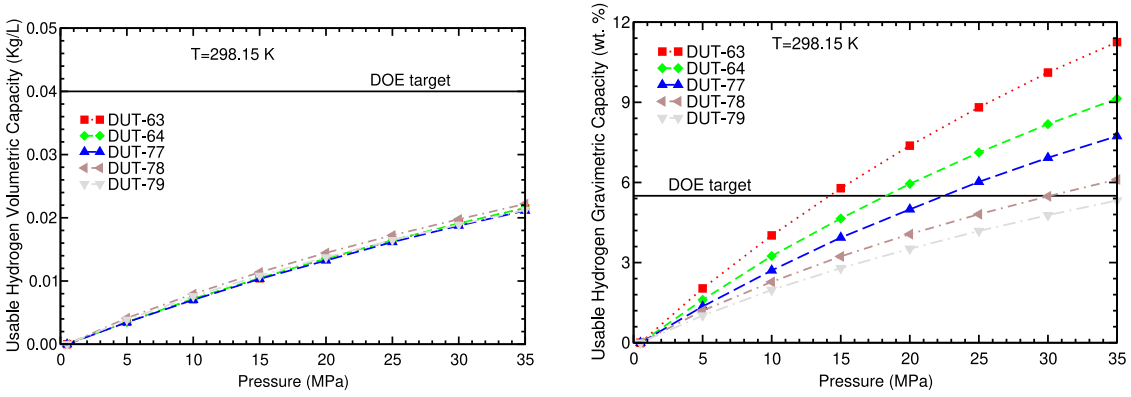

Fig. 4. Hydrogen volumetric and gravimetric usable capacities vs pressure at room temperature of some selected MOFs and the five DUT MOFs.

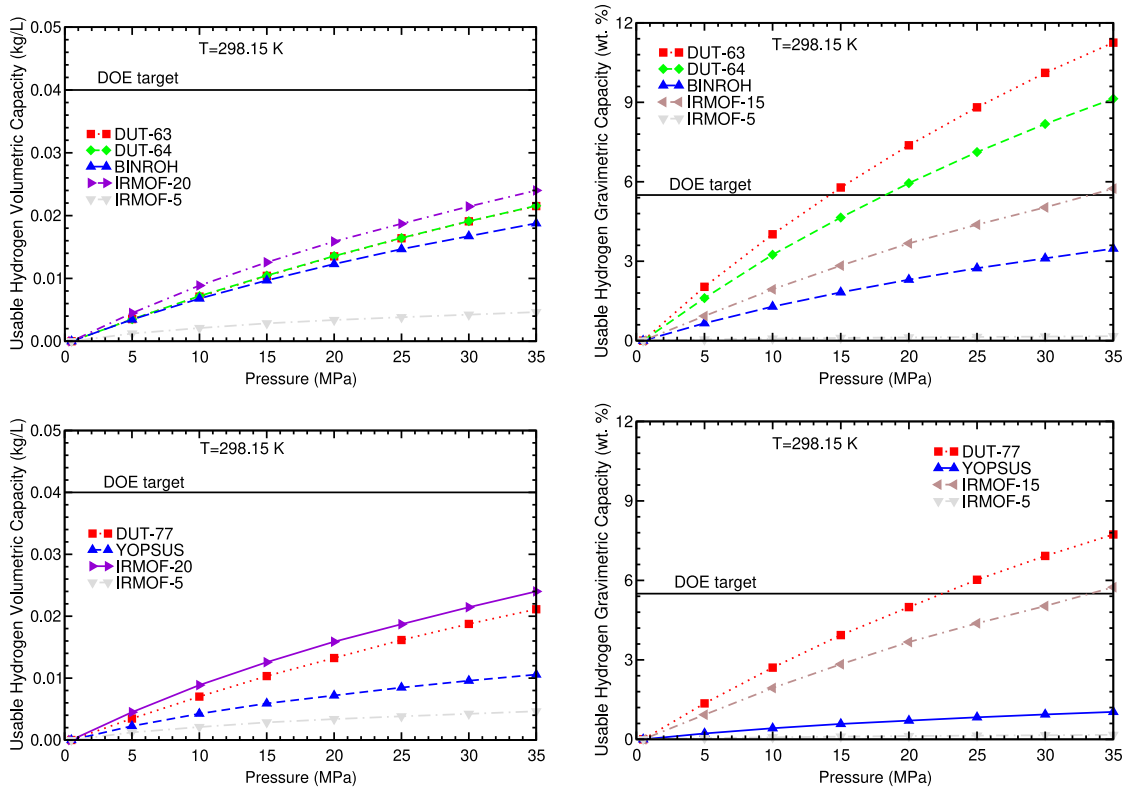

Fig. 5. Hydrogen gravimetric and volumetric usable capacities of DUT-63, 64 and 77, some classical MOFs and the selected Cu-based MOFs with the same C/Cu ratio as DUT-63, 64 and 77, as a function of the pressure, at 298.15 K.

at 298.15 K and 25 MPa on the density, porosity and pore size of the MOFs is plotted in Figs. 7 and 8.

According to Fig. 7, the correlations between the usable methane capacities and the porosity and the density are similar to the ones obtained for hydrogen. Thus, it is important to note that in Fig. 7, the methane usable gravimetric capacities of DUT MOFs are positioned along the general trend line formed by the gravimetric capacities of classical and selected Cu-based MOFs as a function of the density. This suggests that the gravimetric capacities of DUT MOFs can be predicted based on their densities. As regards porosity, the usable methane storage capacities of DUTs, Cu-based MOFs and classical MOFs increase, in general, as the porosity increases. DUTs demonstrate higher gravimetric capacities and slightly lower volumetric capacities compared to MOFs with similar porosities.

Fig. 8 contains the dependence of the usable methane storage capacities on the largest and average pore radius. The methane storage capacities have the same dependence on those two radii as the hydrogen storage capacities. The usable gravimetric capacity is approximately linear with the largest and average pore radius. Similar to the hydrogen case, as the pore radius increases, the density decreases and this causes an increase of the gravimetric capacity. The usable volumetric capacity increases rapidly and reaches a constant or asymptotic value, as the largest and average pore radius increases. The usable methane volumetric capacity can also be approximated by the function $a-b/R$, where R is the largest pore radius R_l or the average pore radius R_{av}.

The classical MOFs with the highest and lowest usable methane storage capacities and the selected Cu-based with the highest capacities and same C/Cu ratio as the DUTs at 25 MPa and room temperature, were chosen for comparison with the DUT MOFs and presented in Tables 8 and 9, similar to the hydrogen case. The methane storage capacities, C/Cu ratios, densities, porosities and pore size of the MOFs obtained in the GCMC simulations at 298.15 K and 25 MPa are presented in Tables 8 and 9. The usable methane gravimetric capacities of

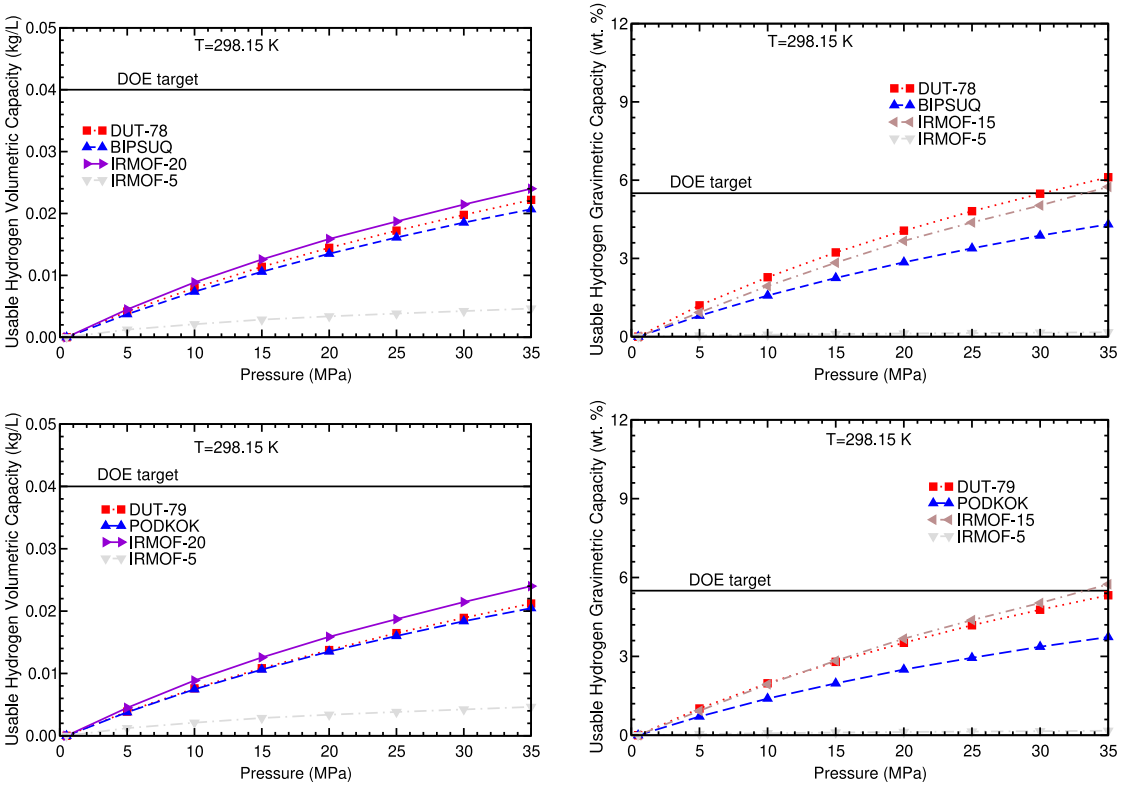

Fig. 6. Hydrogen gravimetric and volumetric usable capacities of DUT-78 and 79, some classical MOFs and the selected Cu-based MOFs with the same C/Cu ratio as DUT-78 and 79, as a function of the pressure, at 298.15 K.

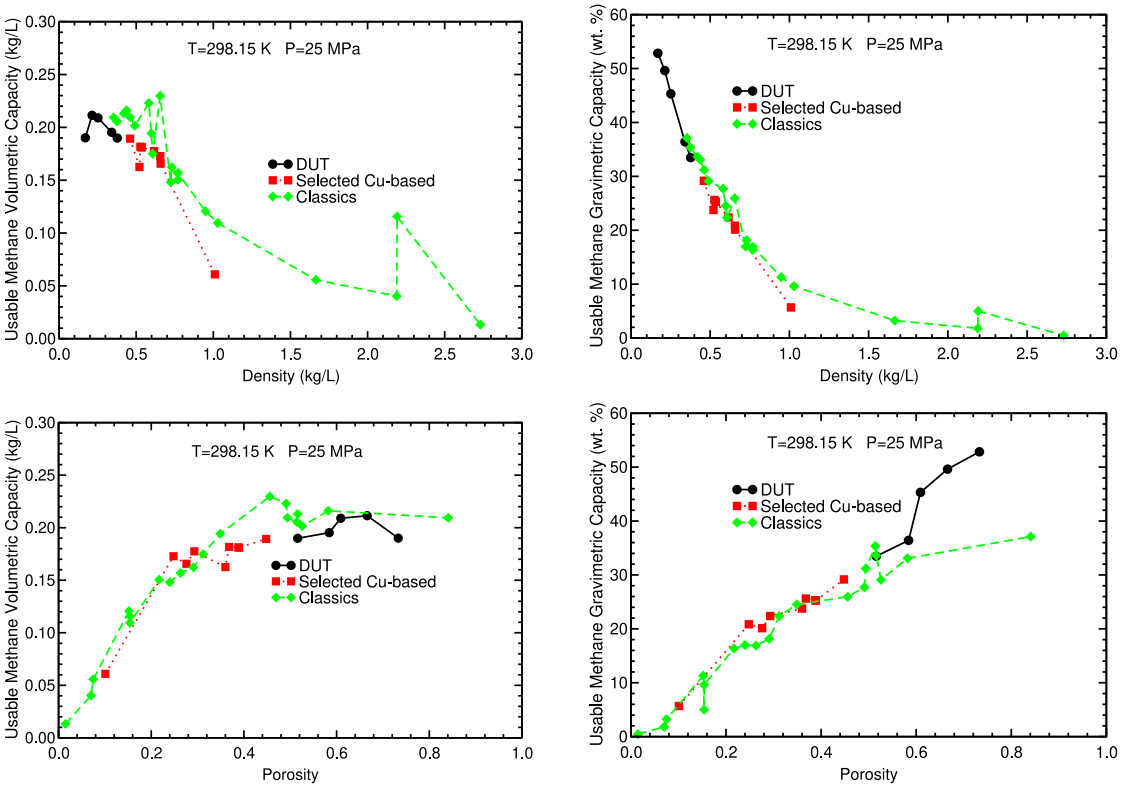

Fig. 7. Methane gravimetric and volumetric usable capacity of DUTs, selected Cu-based MOFs and classical MOFs at 298.15 K and 25 MPa vs density and porosity.

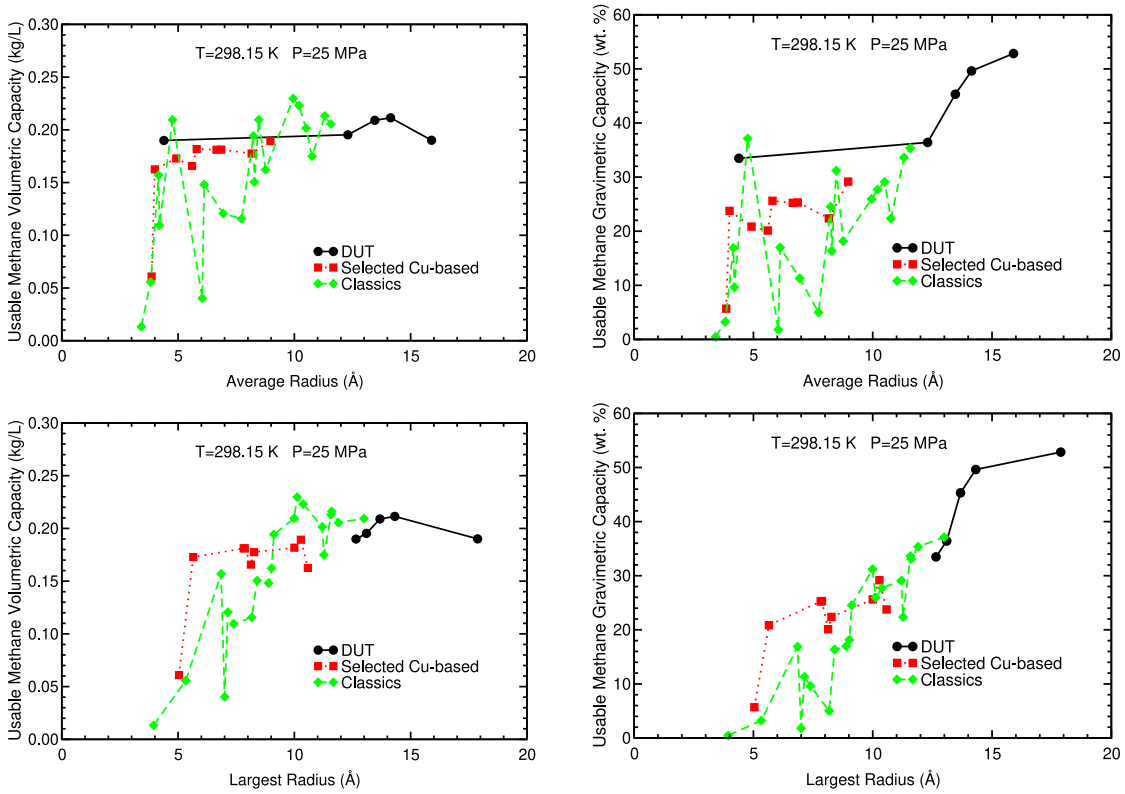

Fig. 8. Usable methane gravimetric and volumetric usable capacity at 298.15 K and 25 MPa vs largest and average pore radius.

Table 8
Methane volumetric (in kg/L) and gravimetric (in wt. %) usable capacities at 298.15 K and 25 MPa obtained in the present GCMC simulations, C/Cu ratio, density (in kg/L), porosity and largest R_l and average R_{av} pore radius (in Å) of the DUT and the selected Cu-based MOFs.

MOF	Ratio C/Cu	v_c	g_c	Density	Porosity	R_l	R_{av}
DUT-63	26	0.190	52.8	0.170	0.733	17.88	15.90
DUT-64	26	0.211	49.6	0.214	0.666	14.32	14.14
DUT-77	32	0.209	45.3	0.252	0.609	13.68	13.46
DUT-78	11.67	0.195	36.4	0.341	0.584	13.10	12.30
DUT-79	13.67	0.190	33.5	0.377	0.516	12.65	4.39
BINROH	26	0.163	23.8	0.521	0.360	10.58	4.00
YOPSUS	32	0.061	5.7	1.010	0.101	5.04	3.86
BIPSUQ	11.43	0.189	29.2	0.460	0.448	10.28	8.97
PODKOK	13.71	0.182	25.6	0.527	0.368	10.00	5.80
ZILFOR	13.5	0.173	20.9	0.656	0.248	5.65	4.92
NIGDIS	13.042	0.166	20.1	0.658	0.276	8.13	5.60
ENIHUG01	13.500	0.178	22.4	0.616	0.293	8.27	8.16
OGEBAF01	11.333	0.181	25.3	0.535	0.388	7.87	6.86
OGEBAF	11.333	0.181	25.2	0.536	0.389	7.82	6.65

DUT MOFs fall within the range of 34–54 wt. %, while the volumetric capacities range from 0.19 to 0.22 kg/L. Among the DUT MOFs, DUT-63 exhibits the highest gravimetric capacity, while having similar volumetric capacity compared to the other DUT MOFs.

A comparison of the usable methane storage capacities at 298.15 and 25 MPa, regardless of the densities and porosities, reveals that the usable methane volumetric capacities of DUTs are high, larger than those of selected Cu-based MOFs and smaller than the highest volumetric capacity of classical MOFs, which corresponds to IRMOF-20 (See Tables 8 and 9). The usable methane gravimetric capacities of DUTs are larger than the gravimetric capacities of Cu-based MOFs. DUT-63, 64 and 77 have usable methane gravimetric capacities larger than the highest gravimetric capacity of the classical MOFs.

Table 9
Methane volumetric (in kg/L) and gravimetric (in wt. %) usable capacities at 298.15 K and 25 MPa obtained in the present GCMC simulations, C/Cu ratio, density (in kg/L), porosity and largest R_l and average R_{av} pore radius (in Å) of the classical MOFs.

MOF	v_c	g_c	Density	Porosity	R_l	R_{av}
IRMOF-5	0.013	0.5	2.731	0.015	3.95	3.42
IRMOF-15	0.209	37.1	0.354	0.841	12.99	4.76
IRMOF-20	0.230	26.0	0.655	0.456	10.12	9.95
IRMOF-1	0.194	24.5	0.598	0.349	9.12	8.24
IRMOF-2	0.116	5.01	2.191	0.154	8.17	7.73
IRMOF-3	0.162	18.2	0.731	0.291	9.02	8.76
IRMOF-4	0.040	1.81	2.189	0.070	7.00	6.04
IRMOF-6	0.148	17.0	0.724	0.240	8.89	6.12
IRMOF-7	0.056	3.24	1.665	0.075	5.33	3.82
IRMOF-8	0.223	27.7	0.582	0.491	10.38	10.20
IRMOF-9	0.157	16.90	0.771	0.263	6.85	4.16
IRMOF-11	0.202	29.1	0.491	0.526	11.20	10.50
IRMOF-12	0.213	33.6	0.420	0.516	11.58	11.31
IRMOF-14	0.206	35.4	0.376	0.514	11.90	11.57
IRMOF-16	0.216	33.1	0.437	0.582	11.61	11.61
IRMOF-18	0.151	16.4	0.770	0.217	8.40	8.28
HKUST-1	0.121	11.3	0.949	0.152	7.14	6.94
MOF-177	0.210	31.2	0.462	0.494	9.99	8.47
NU-111	0.185	30.1	0.430	0.456	12.12	5.99
NU-125	0.175	22.4	0.607	0.312	11.27	10.76
ZIF-8	0.110	9.62	1.029	0.154	7.39	4.20

3.2.2. *Methane storage capacities as a function of pressure*

GCMC simulations were conducted to determine the usable methane storage capacities of DUT MOFs, selected Cu-based MOFs and classical MOFs at 298.15 K and across a range of pressures from 0.5 to 35 MPa. The results of these simulations are depicted in Figs. 9–11. It is important to notice in Fig. 9 that DUT-63 and DUT-64 achieve the desired usable methane gravimetric DOE target, 33.3 wt. %, [10–12] at 298.15 K and 8 MPa. Additionally, DUT-77, DUT-78 and DUT-79 meet this target at 9, 16, and 25 MPa, respectively.

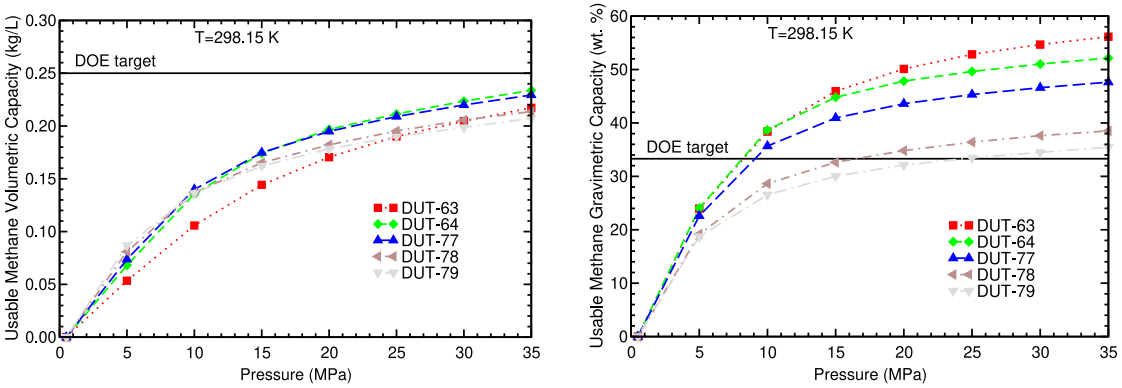

Fig. 9. Methane usable volumetric and gravimetric capacities vs pressure of the five DUT MOFs at room temperature.

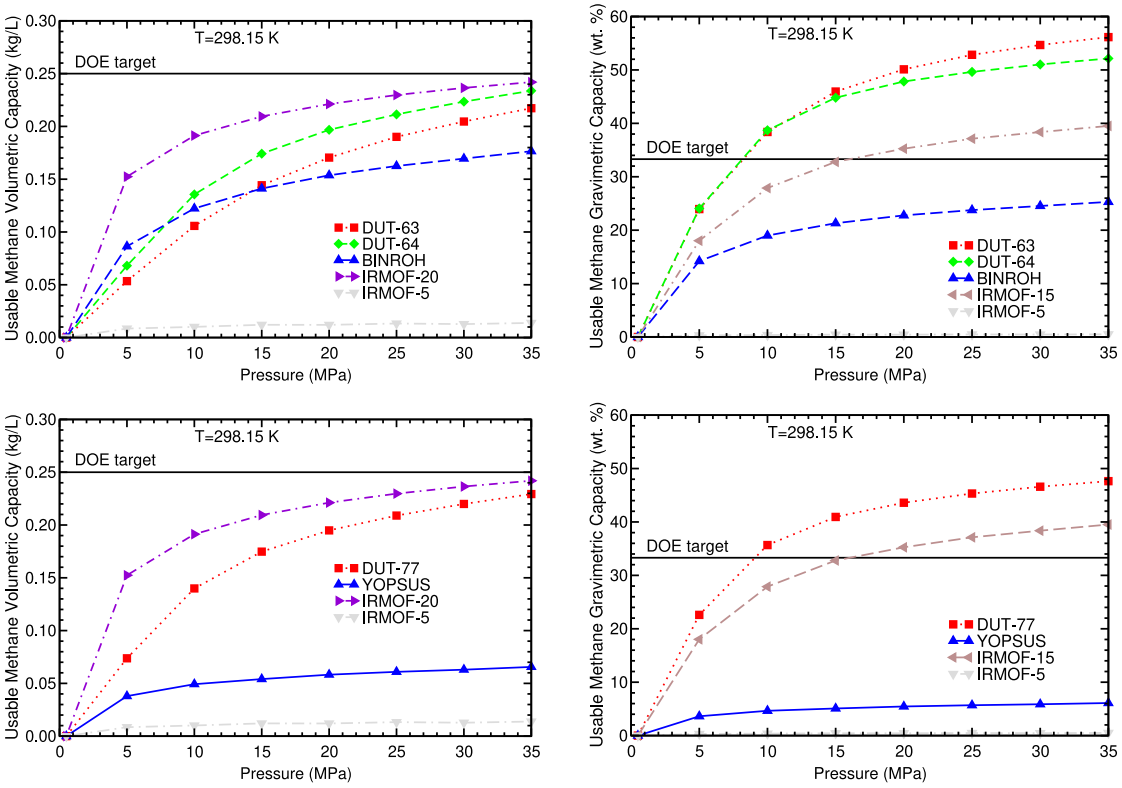

Fig. 10. Methane gravimetric and volumetric usable capacities of DUT-63, 64 and 77, some classical MOFs and the selected Cu-based MOFs with the same C/Cu ratio as DUT-63, 64 and 77, as a function of the pressure, at 298.15 K.

In terms of volumetric capacities, the five DUT MOFs exhibit a consistent trend with similar values (See Fig. 9). At 298.15 K and pressures ranging from 0.5 to 35 MPa, DUT-64 and DUT-77 demonstrate the highest volumetric capacities, reaching around 0.23 kg/L at 35 MPa, which is very close to the DOE target of 0.25 kg/L [10–12]. The volumetric capacities of DUT-63, DUT-78, and DUT-79 at 35 MPa and room temperature are slightly lower than those of DUT-64 and DUT-77, with values ranging from approximately 0.21 to 0.22 kg/L, also very close to the DOE target.

Figs. 10 and 11 show a comparison of the gravimetric and volumetric usable capacities of DUTs and Cu-based MOFs with the same C/Cu ratio and the storage capacities of the classical MOFs with the lowest and highest capacities, as the pressure varies between 0.5 and 35 MPa. Only the selected Cu-based MOF with the highest storage capacities and same ratio is compared in those Figures.

The gravimetric and volumetric storage capacities of DUTs are larger, in general, than those of Cu-based MOFs with the same C/Cu ratio. The volumetric capacities of DUT-78 and 79 are slightly smaller than those of the Cu-based MOFs with their same C/Cu ratio. The comparison with the storage capacities of classical MOFs indicate that the gravimetric capacities of DUT-63, 64 and 77 are larger than the gravimetric capacity of the best classical MOF, while the gravimetric capacities of DUT-78 and 79 are similar or smaller than the gravimetric capacity of the best classical MOF. As regards volumetric capacities, the DUTs have smaller volumetric capacities than the best classical MOF (See Figs. 10 and 11).

4. Conclusions

The present GCMC results are predictions of the usable hydrogen and methane storage capacities at pressures between 0.5 and 35 MPa and room temperature of five DUT MOFs synthesized by a group of the Dresden University of Technology [62]. According to the present GCMC simulations, the five DUT MOFs show high hydrogen and methane

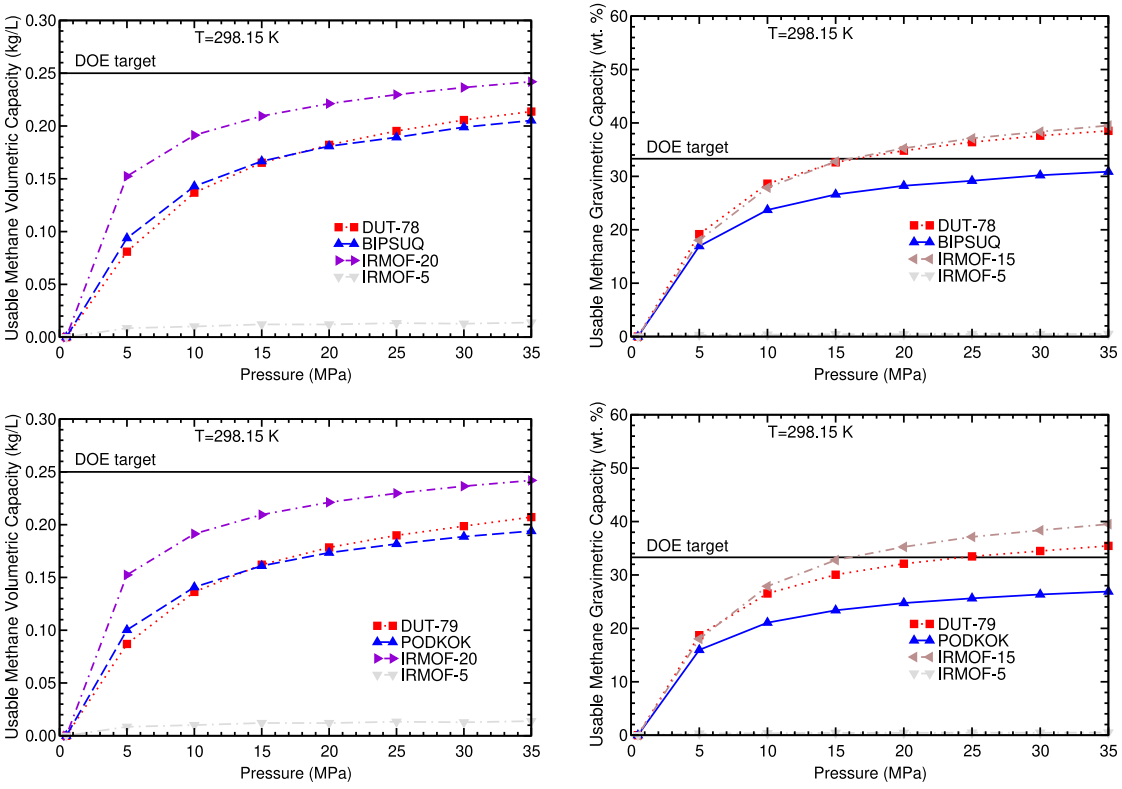

Fig. 11. Methane gravimetric and volumetric usable capacities of DUT-78 and 79, some classical MOFs and the selected Cu-based MOFs with the same C/Cu ratio as DUT-78 and 79, as a function of the pressure, at 298.15 K.

storage capacities at room temperature and pressures of 25–35 MPa, comparable or larger than those of the best classical MOFs and the best Cu-based MOFs.

The dependence of the usable (hydrogen and methane) volumetric and gravimetric storage capacities of the MOFs studied (classical, Cu-based and the novel DUT MOFs) on the porosity, density and the pore radius has been studied. The analysis reveals that the capacities are, in general, inversely proportional to the density and proportional to the porosity. The usable gravimetric capacity is, in general, proportional to the pore radius. The usable volumetric capacity increases rapidly as the pore radius increases and reaches an asymptotic value. The origin of the high capacities of these novel MOFs are their high porosity, low density and relatively wide pores. Their capacities could be improved by doping these novel MOFs with some light elements.

The present GCMC results show that the DUTs have, in general, hydrogen and methane usable gravimetric capacities larger than those of the Cu-based MOFs and classical MOFs. The DUTs have usable hydrogen and methane volumetric capacities that are, in general, comparable or larger than those of Cu-based MOFs and classical MOFs. The best classical MOFs still have larger hydrogen and methane usable volumetric capacities than the DUTs.

The usable hydrogen gravimetric and volumetric storage capacities of the five DUT MOFs at 298.15 K and 25 MPa are in the range 4–9 wt. % and 0.016–0.017 kg/L, respectively. It is important to note that DUT-63 and 64 reach the usable hydrogen gravimetric capacity DOE target, 5.5 wt. %, [7,8] at 17 MPa and room temperature. All the DUT MOFs reach the usable hydrogen gravimetric capacity DOE target at 35 MPa and room temperature.

The usable methane gravimetric and volumetric storage capacities at room temperature and 25 MPa of the DUTs are in the interval 33–53 wt. % and 0.16–0.21 kg/L, respectively. All DUTs reach the usable methane gravimetric capacity DOE target, 33.3 wt. %, [10–12] at 25 MPa and room temperature. The usable methane volumetric capacities of the five DUTs are about 0.21–0.23 kg/L at 35 MPa and room temperature, close to the volumetric capacity DOE target, 0.25 kg/L [10–12]. Hence, according to the present GCMC simulations, these DUTs could be used as adsorbent materials in the tanks of an ANG vehicle, using a pressure of 35 MPa.

Declaration of competing interest

The authors declare that they have no known competing financial interests or personal relationships that could have appeared to influence the work reported in this paper.

Acknowledgments

This work has been funded by the MICINN research project from Spain (Grant PGC2018-093745-B-I00), the Junta de Castilla y León (Grant VA124G18), and the University of Valladolid, Spain. The authors gratefully acknowledge the financial support provided by these institutions, which made this research possible. The authors would also like to express their appreciation for the use of the computer facilities at the Centro de Procesado de Datos - Parque Científico of the University of Valladolid.

References

[1] Chakraborty S, Dash SK, Elavarasan RM, Kaur A, Elangovan D, Meraj ST, Kasinathan P, Said Z. Hydrogen energy as future of sustainable mobility. Front Energy Res 2022;10:893475. http://dx.doi.org/10.3389/fenrg.2022.893475.

[2] Schlichtenmayer M, Hirscher M. The usable capacity of porous materials for hydrogen storage. Appl Phys A 2016;122:379. http://dx.doi.org/10.1007/s00339-016-9864-6.

[3] Jena P. Materials for hydrogen storage: Past, present, and future. J Phys Chem Lett 2011;2(3):206–11. http://dx.doi.org/10.1021/jz1015372.

[4] Broom DP, Webb CJ, Webb KE, Parilla PA, Gennett T, Brown CM, Zacharia R, Tylianakis E, Klontzas E, Froudakis GE, Steriotis TA, Trikalitis PN, Anton DL, Hardy B, Tamburello D, Corgnale C, van Hassel BA, Cossement D, Chahine R, Hirscher M. Outlook and challenges for hydrogen storage in nanoporous materials. Appl Phys A 2021;122:151. http://dx.doi.org/10.1007/s00339-016-9651-4.

[5] Breeze P. Hydrogen energy storage. In: Power system energy storage technologies. London: Elsevier; 2018, p. 69–77, (Chapter 8).
[6] Ding F, Yakobson BI. Challenges in hydrogen adsorptions: from physisorption to chemisorption. Front Phys 2011;6:142–50. http://dx.doi.org/10.1007/s11467-011-0171-6.
[7] Office of Energy Efficiency & Renewable Energy, Fuel Cell Technologies Office. DOE technical targets for onboard hydrogen storage for light-duty vehicles. 2018, https://www.energy.gov/eere/fuelcells/doe-technical-targets-onboard-hydrogen-storage-light-duty-vehicles, Accessed October 27, 2023.
[8] Allendorf MD, Hulvey Z, Gennett T, Ahmed A, Autrey T, Camp J, Cho ES, Furukawa H, Haranczyk M, Head-Gordon M, Jeong S, Karkamkar A, Liu D-J, Long JR, Meihaus KR, Nayyar IH, Nazarov R, Siegel DJ, Stavila V, Urban JJ, Veccham SP, Wood BC. An assessment of strategies for the development of solid-state adsorbents for vehicular hydrogen storage. Energy Environ Sci 2018;11:2784–812. http://dx.doi.org/10.1039/C8EE01085D.
[9] Sherburne M. Natural gas could bridge gap from gasoline to electric vehicles, thanks to metal-organic frameworks. 2022, https://news.umich.edu/natural-gas-could-bridge-gap-from-gasoline-to-electric-vehicles-thanks-to-metal-organic-frameworks, Accessed October 27, 2023.
[10] Advanced Research Projects Agency - Energy, DOE. Methane opportunities for vehicular energy (MOVE) program overview. 2012, http://arpa-e.energy.gov/sites/default/files/documents/files/MOVE_ProgramOverview.pdf, Accessed October 27, 2023.
[11] Advanced Research Projects Agency - Energy, DOE. Methane opportunities for vehicular energy (MOVE) program overview. 2012, https://arpa-e.energy.gov/technologies/programs/move, Accessed October 27, 2023.
[12] International Organization for Standardization. ISO 15403-1:2006(en) Natural gas — Natural gas for use as a compressed fuel for vehicles — Part 1: Designation of the quality. 2006, https://www.iso.org/obp/ui/#iso:std:iso:15403:-1:ed-1:v1:en, Accessed October 27, 2023.
[13] Beckner M, Dailly A. Adsorbed methane storage for vehicular applications. Appl Energy 2015;149:69–74. http://dx.doi.org/10.1016/j.apenergy.2015.03.123.
[14] Yabing H, Zhou W, Guodong Q, Chen B. Methane storage in metal-organic frameworks. Chem Soc Rev 2014;45:5657–78.
[15] Office of Energy Efficiency & Renewable Energy, Hydrogen and Fuel Cell Technologies Office. High-pressure hydrogen tank testing. 2022, https://www.energy.gov/eere/fuelcells/high-pressure-hydrogen-tank-testing, Accessed October 27, 2023.
[16] Macili A, Vlamidis Y, Pfusterschmied G, Leitgeb M, Schmid U, Heun S, Veronesi S. Study of hydrogen absorption in a novel three-dimensional graphene structure: Towards hydrogen storage applications. Appl Surf Sci 2023;615:156375. http://dx.doi.org/10.1016/j.apsusc.2023.156375.
[17] Zhang Y, Zhang L, Pan H, Wang H, Li Q. Li-decorated porous hydrogen substituted graphyne: A new member of promising hydrogen storage medium. Appl Surf Sci 2021;535:147683. http://dx.doi.org/10.1016/j.apsusc.2020.147683.
[18] Karki S, Chakraborty SN. A Monte Carlo simulation study of hydrogen adsorption in slit-shaped pores. Microporous Mesoporous Mater 2021;317:110970. http://dx.doi.org/10.1016/j.micromeso.2021.110970.
[19] Kessler C, Eller J, Gross J, Hansen N. Adsorption of light gases in covalent organic frameworks: comparison of classical density functional theory and grand canonical Monte Carlo simulations. Microporous Mesoporous Mater 2021;324:111263. http://dx.doi.org/10.1016/j.micromeso.2021.111263.
[20] Xu W, Chen Y, Song M, Liu X, Zhao Y, Zhang M, Zhang C. First-principles study on methane (CH_4) storage properties of graphdiyne. J Phys Chem C 2020;124(15):8110–8. http://dx.doi.org/10.1021/acs.jpcc.9b12009.
[21] Wang Y, Xu G, Deng S, Wu Q, Meng Z, Huang X, Bi L, Yang Z, Lu R. Lithium and sodium decorated graphdiyne as a candidate for hydrogen storage: First-principles and grand canonical Monte Carlo study. Appl Surf Sci 2020;509:144855. http://dx.doi.org/10.1016/j.apsusc.2019.144855.
[22] Wang Y, Wu Q, Deng S, Ma R, Huang X, Bi L, Yang Z. Hydrogen storage in Na-decorated h_4,4,4-graphyne: A density functional theory and Monte Carlo study. Appl Surf Sci 2019;495:143621. http://dx.doi.org/10.1016/j.apsusc.2019.143621.
[23] Cheng Y-H, Zhang C-Y, Ren J, Tong K-Y. Hydrogen storage in Li-doped fullerene-intercalated hexagonal boron nitrogen layers. Front Phys 2016;11(5):113101. http://dx.doi.org/10.1007/s11467-016-0559-4.
[24] Blanco AAG, Vallone AF, Korili SA, Gil A, Sapag K. A comparative study of several microporous materials to store methane by adsorption. Microporous Mesoporous Mater 2016;224:323–31.
[25] Hassani A, Mosavian HMT, Ahmadpour A, Farhadian N. Hybrid molecular simulation of methane storage inside pillared graphene. J Chem Phys 2015;142(23):234704. http://dx.doi.org/10.1063/1.4922541.
[26] Chouhan RK, Ulman K, Narasimhan S. Graphene oxide as an optimal candidate material for methane storage. J Chem Phys 2015;143(4):044704. http://dx.doi.org/10.1063/1.4927141.
[27] Zhou X, Zhou J, Sun Q. Tripyrrylmethane based 2D porous structure for hydrogen storage. Front Phys 2011;6:220–3. http://dx.doi.org/10.1007/s11467-011-0176-1.
[28] Li S, m Zhao H, Jena P. Ti-doped nano-porous graphene: A material for hydrogen storage and sensor. Front Phys 2011;6:204–8. http://dx.doi.org/10.1007/s11467-011-0178-z.
[29] Rahmati M, Modarress H. Grand canonical Monte Carlo simulation of isotherm for hydrogen adsorption on nanoporous siliceous zeolites at room temperature. Appl Surf Sci 2009;255(9):4773–8. http://dx.doi.org/10.1016/j.apsusc.2008.11.072.
[30] Yuan X, Cheng J, Fang X, Wang Z, Wang X. Monte Carlo simulation of hydrogen physisorption in K-doped single walled carbon nanotube array. Appl Surf Sci 2009;255(18):8122–5. http://dx.doi.org/10.1016/j.apsusc.2009.05.028.
[31] Li J, Furuta T, Goto H, Ohashi T, Fujiwara Y, Yip S. Theoretical evaluation of hydrogen storage capacity in pure carbon nanostructures. J Chem Phys 2003;119(4):2376–85. http://dx.doi.org/10.1063/1.1582831.
[32] Jose R, Bangar G, Pal S, Rajaraman G. Role of molecular modelling in the development of metal-organic framework for gas adsorption applications. J Chem Sci 2023;135:19. http://dx.doi.org/10.1007/s12039-022-02130-5.
[33] Nath K, Ahmed A, Siegel DJ, Matzger AJ. Computational identification and experimental demonstration of high-performance methane sorbents. Angew Chem Int Edn 2022;61(25):e202203575. http://dx.doi.org/10.1002/anie.202203575.
[34] Zhao D, Wang X, Yue L, He Y, Chen B. Porous metal–organic frameworks for hydrogen storage. Chem Commun 2022;58:11059–78. http://dx.doi.org/10.1039/D2CC04036K.
[35] Li A. Metal-organic frameworks-based hydrogen storage strategies and applications. J Phys: Conf Ser 2022;2403(1):012022. http://dx.doi.org/10.1088/1742-6596/2403/1/012022.
[36] Suresh K, Aulakh D, Purewal J, Siegel DJ, Veenstra M, Matzger AJ. Optimizing hydrogen storage in MOFs through engineering of crystal morphology and control of crystal size. J Am Chem Soc 2021;143(28):10727–34. http://dx.doi.org/10.1021/jacs.1c04926.
[37] Zhang X, Lin R-B, Wang J, Wang B, Liang B, Yildirim T, Zhang J, Zhou W, Chen B. Optimization of the pore structures of MOFs for record high hydrogen volumetric working capacity. Adv Mater 2020;32(17):1907995. http://dx.doi.org/10.1002/adma.201907995.
[38] Broom DP, Webb CJ, Fanourgakis GS, Froudakis GE, Trikalitis PN, Hirscher M. Concepts for improving hydrogen storage in nanoporous materials. Int J Hydrog Energy 2019;44(15):7768–79. http://dx.doi.org/10.1016/j.ijhydene.2019.01.224.
[39] Kim J, Yeo S, Jeon J-D, Kwak S-Y. Enhancement of hydrogen storage capacity and hydrostability of metal–organic frameworks (MOFs) with surface-loaded platinum nanoparticles and carbon black. Microporous Mesoporous Mater 2015;202:8–15. http://dx.doi.org/10.1016/j.micromeso.2014.09.025.
[40] Rydén J, Öberg S, Heggie M, Rayson M, Briddon P. Hydrogen storage in the manganese containing metal–organic framework MOF-73. Microporous Mesoporous Mater 2013;165:205–9. http://dx.doi.org/10.1016/j.micromeso.2012.08.024.
[41] Hirscher M, Panella B, Schmitz B. Metal-organic frameworks for hydrogen storage. Microporous Mesoporous Mater 2010;129(3):335–9. http://dx.doi.org/10.1016/j.micromeso.2009.06.005.
[42] Donà L, Brandenburg JG, Civalleri B. Metal-organic frameworks properties from hybrid density functional approximations. J Chem Phys 2022;156(9):094706. http://dx.doi.org/10.1063/5.0080359.
[43] Fanourgakis GS, Gkagkas K, Froudakis G. Introducing artificial MOFs for improved machine learning predictions: Identification of top-performing materials for methane storage. J Chem Phys 2022;156(5):054103. http://dx.doi.org/10.1063/5.0075994.
[44] Fei S, Alizadeh A, Hsu W-L, Delaunay J-J, Daiguji H. Analysis of the water adsorption mechanism in metal–organic framework MIL-101(Cr) by molecular simulations. J Phys Chem C 2021;125(48):26755–69. http://dx.doi.org/10.1021/acs.jpcc.1c06917.
[45] Forrest KA, Verma G, Ye Y, Ren J, Ma S, Pham T, Space B. Methane storage in flexible and dynamical metal–organic frameworks. Chem Phys Rev 2022;3(2):021308. http://dx.doi.org/10.1063/5.0072805.
[46] Li F-G, Liu C, Yuan D, Dai F, Wang R, Wang Z, Lu X, Sun D. Ultrahigh hydrogen uptake in an interpenetrated Zn_4O-based metal-organic framework. CCS Chem 2022;4(3):832–7. http://dx.doi.org/10.31635/ccschem.021.202000738.
[47] Peedikakkal AMP, Aljundi IH. Upgrading the hydrogen storage of MOF-5 by post-synthetic exchange with divalent metal ions. Appl Sci 2021;11(24):11687. http://dx.doi.org/10.3390/app112411687.
[48] Mason JA, Oktawiec J, Taylor MK, Hudson MR, Rodriguez J, Bachman JE, Gonzalez MI, Cervellino A, Guagliardi A, Brown CM, Llewellyn PL, Masciocchi N, Long JR. Methane storage in flexible metal–organic frameworks with intrinsic thermal management. Nature 2015;527:357–61. http://dx.doi.org/10.1038/nature15732.
[49] Zhang G, Liang Y, Cui G, Dou B, Lu W, Yang Q, Yan X. Grand canonical Monte Carlo simulation of the adsorption and separation of carbon dioxide and methane using functionalized Mg-MOF-74. Energy Rep 2023;9:2852–60. http://dx.doi.org/10.1016/j.egyr.2023.01.121.
[50] Yu Y, Shang M, Kong L, Wang L, Sun T. Influence of ligands within Al-based metal-organic frameworks for selective separation of methane from unconventional natural gas. Chemosphere 2023;321:138160. http://dx.doi.org/10.1016/j.egyr.2023.01.121.

[51] Yeh C-H, Khan AH, Miyazak T, Jiang J-C. The investigation of methane storage at the Ni-MOF-74 material: a periodic DFT calculation. Phys Chem Chem Phys 2021;23:12270–9. http://dx.doi.org/10.1039/D1CP01276B.
[52] Li D-Z, Chen L, Liu G, Yuan Z-Y, Li B-F, Zhang X, Wei J-Q. Porous metal–organic frameworks for methane storage and capture: status and challenges. New Carbon Mater 2021;36(3):468–96. http://dx.doi.org/10.1016/S1872-5805(21)60034-3.
[53] Rosen AS, Notestein JM, Snurr RQ. Structure–activity relationships that identify metal–organic framework catalysts for methane activation. ACS Catal 2019;9(4):3576–87. http://dx.doi.org/10.1021/acscatal.8b05178.
[54] Tsivion E, Mason JA, Gonzalez MI, Long JR, Head-Gordon M. A computational study of CH_4 storage in porous framework materials with metalated linkers: connecting the atomistic character of CH_4 binding sites to usable capacity. Chem Sci 2016;7:4503–18. http://dx.doi.org/10.1039/C6SC00529B.
[55] Sur M, Dornfeld M, Ganz E. Calculation of hydrogen storage capacity of metal-organic and covalent-organic frameworks by spillover. J Chem Phys 2009;131(17):174703. http://dx.doi.org/10.1063/1.3257737.
[56] Samanta A, Furuta T, Li J. Theoretical assessment of the elastic constants and hydrogen storage capacity of some metal-organic framework materials. J Chem Phys 2006;125(8):084714. http://dx.doi.org/10.1063/1.2337287.
[57] Sagara T, Ortony J, Ganz E. New isoreticular metal-organic framework materials for high hydrogen storage capacity. J Chem Phys 2005;123(21):214707. http://dx.doi.org/10.1063/1.2133734.
[58] Sagara T, Klassen J, Ganz E. Computational study of hydrogen binding by metal-organic framework-5. J Chem Phys 2004;121(24):12543–7. http://dx.doi.org/10.1063/1.1809608.
[59] Ahmed A, Seth S, Purewal J, Wong-Foy AG, Veenstra M, Matzger AJ, Siegel DJ. Exceptional hydrogen storage achieved by screening nearly half a million metal-organic frameworks. Nature Commun 2019;10:1568. http://dx.doi.org/10.1038/s41467-019-09365-w.
[60] Fu J, Tian Y, Wu J. Seeking metal–organic frameworks for methane storage in natural gas vehicles. Adsorption 2015;21. http://dx.doi.org/10.1007/s10450-015-9688-2, 499–507.
[61] Basdogan Y, Keskin S. Simulation and modelling of MOFs for hydrogen storage. CrystEngComm 2015;17:261–75. http://dx.doi.org/10.1039/C4CE01711K.
[62] Müller P, Grünker R, Volodymyr B, Pfeffermann M, Senkovska I, Weiss MS, Feng X, Kaskeli S. Topological control of 3,4-connected frameworks based on the Cu2-paddle-wheel node: tbo or pto, and why? J Chem Phys 2016;18:8164–71. http://dx.doi.org/10.1039/C6CE01513A.
[63] Metropolis N. The beginning of the Monte Carlo method. Los Alamos Sci 1987;15:125–30.
[64] Soave G. Equilibrium constants from a modified Redlich-Kwong equation of state. Chem Eng Sci 1972;27:1197–203.
[65] Zhou L, Zhou Y. Determination of compressibility factor and fugacity coefficient of hydrogen in studies of adsorptive storage. Int J Hydrog Energy 2001;26:597–601.
[66] Xu X-H, Duan Y-Y, Yang Z. Crossover volume translation Soave-Redlich-Kwong equation of state for fluids. Ind Eng Chem Res 2012;51:6580–5.
[67] Lennard-Jones JE. On the determination of molecular fields. Proc R Soc (Lond) A 1924;106:463–77. http://dx.doi.org/10.1098/rspa.1924.0082.
[68] Berthelot D. Sur le mélange des gaz. C R Hebd Séances L'Acad Sci 1898;126:1703.
[69] Good RJ, Hope CJ. New combining rule for intermolecular distances in intermolecular potential functions. J Chem Phys 1970;53:540–3. http://dx.doi.org/10.1063/1.1674022.
[70] Rzepka M, Lamp P, de la Casa-Lillo MA. Physisorption of hydrogen on microporous carbon nanotubes. J Phys Chem B 1998;102:10894–8.
[71] Feynman RP, Hibbs A. Quantum mechanics and path integrals. New York: McGraw-Hill; 1965.
[72] Caviedes D, Cabria I. Grand canonical Monte Carlo simulations of the hydrogen storage capacities of slit-shaped pores, nanotubes and torusenes. Int J Hydrog Energy 2022;47:11916–28. http://dx.doi.org/10.1016/j.ijhydene.2022.01.229.
[73] Cabria I. Grand canonical Monte Carlo simulations of the hydrogen and methane storage capacities of novel but MOFs at room temperature. Int J Hydrog Energy 2023. http://dx.doi.org/10.1016/j.ijhydene.2023.06.298.
[74] Docherty H, Galindo A, Vega C, Sanz E. A potential model for methane in water describing correctly the solubility of the gas and the properties of the methane hydrate. J Chem Phys 2006;125(7):074510. http://dx.doi.org/10.1063/1.2335450.
[75] Filippova VP, Kunavin SA, Pugachev MS. Calculation of the parameters of the Lennard-Jones potential for pairs of identical atoms based on the properties of solid substances. Inorg Mater Appl Res 2015;6:1–4.
[76] Mayo SL, Olafson BD, Goddard III WA. DREIDING: A generic force field. J Phys C: Solid State Phys 1990;94:8897–909.
[77] Tu Y, Xiu P, Wan R, Hu J, Zhou R, Fang H. Water-mediated signal multiplication with Y-shaped carbon nanotubes. Proc Natl Acad Sci USA 2009;106:18120–4.
[78] Cheung PSY, Powles JG. The properties of liquid nitrogen. Mol Phys 1975;30:921–49.
[79] Jorgensen WL, Madura JD, Swenson CJ. Optimized intermolecular potential functions for liquid hydrocarbons. J Am Chem Soc 1984;106:6638–46.
[80] Soper AK. The structure of molten $ZnCl_2$: A new analysis of some old data. Pramana J Phys 2004;63:41–50.
[81] Zeo++: an open source software for performing high-throughput geometry-based analysis of porous materials and their voids. Last version: June 20, 2017, http://www.zeoplusplus.org, accessed November 13, 2023.
[82] Ongari D, Boyd PG, Barthel S, Witman M, Haranczyk M, Smit B. Accurate characterization of the pore volume in microporous crystalline materials. Langmuir 2017;33(51):14529–38. http://dx.doi.org/10.1021/acs.langmuir.7b01682.
[83] Willems TF, Rycroft CH, Kazi M, Meza JC, Haranczyk M. Algorithms and tools for high-throughput geometry-based analysis of crystalline porous materials. Microporous Mesoporous Mater 2012;149(1):134–41. http://dx.doi.org/10.1016/j.micromeso.2011.08.020.
[84] Zhang J, Song C, Zhang J, Baker R, Zhang L. Understanding the effects of backpressure on PEM fuel cell reactions and performance. J Electroanal Chem 2013;688:130–6. http://dx.doi.org/10.1016/j.jelechem.2012.09.033.
[85] 2023. www.ccdc.cam.ac.uk, Accessed October 27, 2023.
[86] Assoualaye G, Tom A, Djongyang N. Monte Carlo study of hydrogen adsorption by MOF-5 doped with cobalt at ambient temperature and pressure. SN Appl Sci 2020;2:1815. http://dx.doi.org/10.1007/s42452-020-03627-9.
[87] Zhou W, Wu H, Hartman MR, Yildirim T. Hydrogen and methane adsorption in metal-organic frameworks: A high-pressure volumetric study. J Phys Chem C 2007;111(44):16131–7. http://dx.doi.org/10.1021/jp074889i.
[88] Rodrigues NM, Politi JR, Martins JB. Are metal dopant and ligands efficient to optimize the adsorption rate of CH_4, H_2 and H_2S on IRMOFs? Insights from factorial design. Comput Mater Sci 2022;210:111438. http://dx.doi.org/10.1016/j.commatsci.2022.111438.
[89] Saha D, Deng S. Hydrogen adsorption on metal-organic framework MOF-177. Tsinghua Sci Technol 2010;15(4):363–76. http://dx.doi.org/10.1016/S1007-0214(10)70075-4.
[90] Peng Y, Krungleviciute V, Eryazici I, Hupp JT, Farha OK, Yildirim T. Methane storage in metal-organic frameworks: Current records, surprise findings, and challenges. J Am Chem Soc 2013;135(32):11887–94. http://dx.doi.org/10.1021/ja4045289.
[91] Alezi D, Jia J, Bhatt PM, Shkurenko A, Solovyeva V, Chen Z, Belmabkhout Y, Eddaoudi M. Reticular chemistry for the construction of highly porous aluminum-based nia-metal-organic frameworks. Inorg Chem 2022;61(28):10661–6. http://dx.doi.org/10.1021/acs.inorgchem.2c00756.
[92] Granja-DelRío A, Cabria I. Grand canonical Monte Carlo simulations of hydrogen and methane storage capacities of two novel Al-nia MOFs at room temperature. Int J Hydrog Energy 2023. http://dx.doi.org/10.1016/j.ijhydene.2023.08.023.
[93] He Y, Guo Z, Xiang S, Zhang Z, Zhou W, Fronczek FR, Parkin S, Hyde ST, O'Keeffe M, Chen B. Metastable interwoven mesoporous metal–organic frameworks. Inorg Chem 2013;52(19):11580–4. http://dx.doi.org/10.1021/ic401870e.
[94] Hou G-G, Ma J-P, Sun T, Dong Y-B, Huang R-Q. A binuclear Cu^{II} metallacycle capable of discerning between pyrazine and its different methyl-substituted derivatives based on reversible intracage Metal–Ligand binding. Chem Eur J 2009;15(10):2261–5. http://dx.doi.org/10.1002/chem.200802690.
[95] Gao W-Y, Wojtas L, Ma S. A porous metal–metalloporphyrin framework featuring high-density active sites for chemical fixation of CO_2 under ambient conditions. Chem Commun 2014;50:5316–8. http://dx.doi.org/10.1039/C3CC47542E.
[96] Barin G, Krungleviciute V, Gomez-Gualdron DA, Sarjeant AA, Snurr RQ, Hupp JT, Yildirim T, Farha OK. Isoreticular series of (3,24)-connected metal–organic frameworks: Facile synthesis and high methane uptake properties. Chem Mater 2014;26(5):1912–7. http://dx.doi.org/10.1021/cm404155s.